Outer Radiation Belt Flux and Phase Space Density Response to Sheath Regions: Van Allen Probes and GPS Observations

Milla M. H. Kalliokoski[1], Michael G. Henderson[2], Steven K. Morley[2], Emilia K. J. Kilpua[1], Adnane Osmane[1], Leonid Olifer[3], Drew L. Turner[4], Allison Jaynes[5], Harriet George[1], Sanni Hoilijoki[1], Lucile Turc[1], Minna Palmroth[1,6]

[1]Department of Physics, University of Helsinki, Helsinki, Finland
[2]Space Science and Applications, Los Alamos National Laboratory, Los Alamos, New Mexico, USA
[3]Department of Physics, University of Alberta, Edmonton, Alberta, Canada
[4]Johns Hopkins University Applied Physics Laboratory, Laurel, Maryland, USA
[5]Department of Physics and Astronomy, University of Iowa, Iowa City, Iowa, USA
[6]Space and Earth Observation Centre, Finnish Meteorological Institute, Helsinki, Finland

Key Points:

- High data density GPS measurements confirm RBSP outer belt electron flux response to ICME-driven sheaths at 6-hour and 30-minute timescales
- PSD response shows that only geoeffective sheaths energize electrons but loss occurs in response to all sheaths
- Impacts in electron flux and PSD presented here are caused by sheaths, and the early ejecta acts to replenish the lost electrons

Corresponding author: M. M. H. Kalliokoski, `milla.kalliokoski@helsinki.fi`

Abstract

Turbulent and compressed sheath regions preceding interplanetary coronal mass ejections (ICMEs) strongly impact electron dynamics in the outer radiation belt. Changes in electron flux can occur on timescales of tens of minutes, which is difficult to capture by a two-satellite mission such as the Van Allen Probes (RBSP). The recently released Global Positioning System (GPS) data set has higher data density owing to the large number of satellites in the constellation equipped with energetic particle detectors. Investigating electron fluxes in a wide range of energies and sheaths observed from 2012 to 2018, we show that the flux response to sheaths on a timescale of 6 hours, previously reported from RBSP data, is reproduced by GPS measurements. Furthermore, GPS data enables derivation of the response on a shorter timescale of 30 minutes, which further confirms that the energy and L-shell dependent changes in electron flux are due to the impact of the sheath. Sheath-driven loss is underestimated over longer timescales as the electrons recover during the ejecta. We additionally show the response of electron phase space density (PSD), which is a key quantity in identifying true loss from the system and electron energization through wave-particle interactions. The PSD response is calculated from both RBSP and GPS data for the 6-hour timescale, as well as from GPS data for the 30-minute timescale. The response is divided based on the geoeffectiveness of the sheaths revealing that electrons are effectively accelerated only during geoeffective sheaths, while loss is commonly caused by all sheaths.

1 Introduction

Electron content in the outer Van Allen radiation belt can undergo dramatic changes on various timescales in response to magnetospheric disturbances (e.g., Reeves et al., 2003; Baker et al., 2014; Turner et al., 2014). One of the key drivers of such disturbances are interplanetary coronal mass ejections (ICMEs) that are large-scale heliospheric structures originating from gigantic eruptions from the Sun (e.g., Kilpua, Balogh, et al., 2017; Kilpua, Koskinen, & Pulkkinen, 2017). ICMEs typically consist of a leading shock and a sheath region followed by the ejecta. The sheath and ejecta have different solar wind properties, which lead to different responses of the radiation belt system (e.g., Kilpua et al., 2015; Turner et al., 2019; Kalliokoski et al., 2020; Kalliokoski et al., 2022). Sheaths are characterized by large amplitude magnetic field fluctuations and high dynamic pressure, and tend to cause intense wave activity in the inner magnetosphere and strong compression of the magnetopause. Thus, sheaths effectively accelerate electrons and scatter them away from the belts (e.g., Kilpua, Turner, et al., 2019; Da Silva et al., 2020; Kalliokoski et al., 2022).

Typically, radiation belt studies consider the overall response of the outer radiation belt to geomagnetic storms. This overall response is estimated by comparing the fluxes before and after the peak of the storm over relatively long time periods (at least half a day or even several days; e.g., O'Brien et al., 2001; Reeves et al., 2003; Turner et al., 2015; Moya et al., 2017; Turner et al., 2019). However, this approach cannot yield information on isolated solar wind structures when they arrive in succession, which is often the case (i.e., a sheath followed by an ejecta, or an ejecta followed by a fast stream), or on localised spatial and temporal responses of the Earth's radiation belts. Kalliokoski et al. (2020) used otherwise similar approach to study the outer belt electron response to ICME sheath regions using the Van Allen Probes data, but compared the fluxes before and after the sheath (instead of around the peak of a storm) and averaged the fluxes over a shorter timescale of 6 hours. This enabled examination of the more immediate electron flux response to the sheath regions and this study revealed a clear energy and L-shell dependency of the response. Sheaths typically enhance electron fluxes at lower energies (10s to 100s keV) and deplete them at higher energies (several 100s keV to several MeV), with both responses being more common at $L > 4$, while the innermost parts of the outer belt remain mostly unchanged. This study, in addition to considering events driving geomagnetic storms, included nongeoeffective sheaths and showed that such events can cause a dramatic radiation belt response as well. A geoeffective sheath was defined as having the SYM-H geomagnetic activity index drop below -30 nT during the sheath or 2 hours after it, while during a nongeoeffective sheath SYM-H remains above -30 nT. This definition is also employed in the current paper.

Case studies of outer belt electron variation have resolved changes on similar or shorter timescales than the 6-hour period studied in Kalliokoski et al. (2020) in response to solar wind transients. Reeves et al. (2013) reported an outer belt electron flux enhancement occurring over 11 hours during a geomagnetic storm but the initial couple of orders of magnitude enhancement was resolved at about 6 hours. Morley, Friedel, Spanswick, et al. (2010) analysed a set of solar wind stream interfaces and found that the median timescale for electron dropouts was about 7 hours. However, even faster changes in the outer belt electron fluxes on timescales of 2 hours or less have been reported. Morley, Friedel, Cayton, and Noveroske (2010) showed about 2 hours for a dropout and Olifer et al. (2018) showed dropouts with timescales from 30 minutes to 2 hours during geomagnetic storms, while enhancements at about 30 minute timescale were presented by Kim et al. (2021). This indicates that, while much shorter than in previous response studies, investigating the radiation belt response over 6 hours might still miss important changes. The Van Allen Probes mission consists of two spacecraft and the data density they supply cannot thus provide more accurate estimations with sufficient L-shell coverage.

An increased temporal resolution and broader spatial coverage given by higher data density has recently been provided by the Global Positioning System (GPS) constellation (Morley et al., 2017). It consists of over 20 satellites currently in orbit. These satellites are equipped with Combined X-ray Dosimeters (CXD), Los Alamos National Laboratory developed and built energetic particle instruments, that measure electrons in the outer radiation belt. A combination of the data from multiple individual GPS satellites provides nearly continuous monitoring of any given L (McIlwain, 1961) or L^* (Roederer, 1970), down to a few tens of minutes temporal resolution (Morley et al., 2016). The downside of GPS satellites in comparison to RBSP is that the sensors can be considered roughly hemispheric measuring particle populations with various pitch angles at once and the satellites are not equipped with magnetometers. Therefore, models for the pitch angle distribution (PAD) and geomagnetic field are needed in order to calculate phase space density. Despite the operational nature of the CXD instruments, the reported omnidirectional fluxes from these instruments have been shown to compare well with observations of the more sophisticated instrumentation on RBSP (Morley et al., 2016).

In this paper, we will first revisit the analysis of outer radiation belt electron flux response to sheaths derived from RBSP observations by Kalliokoski et al. (2020). We then reproduce this analysis using data from the GPS constellation. We will investigate both differences and similarities in the response using the same 6-hour averaging for RBSP and GPS data, and then repeat the analysis with GPS for temporal resolution of only 30 minutes. Then, we will perform a similar response analysis with electron phase space density (PSD), which allows us to reveal the dependencies of non-adiabatic acceleration and loss on the first adiabatic invariant and L^*. Again 6-hour averaging is used for RBSP data and both 6-hour and 30-minute averaging are used for the GPS data. This part of the study also differentiates between geoeffective and nongeoeffective events, as defined above. More broadly, this approach will demonstrate the applicability of the GPS data in scientific analysis, highlight the advantages and shortcomings of these two data sets, and emphasize their combined potential for many future studies. The RBSP and GPS data and the methodology to calculate fluxes and PSD from them are described in Section 2. Sections 3 and 4 present the response analysis results calculated for fluxes and PSD, respectively. We discuss the results in Section 5 and summarise in Section 6.

2 Comparison of Van Allen Probes and GPS Data and Methods

2.1 Van Allen Probes and GPS

The Van Allen Probes (RBSP) were a scientific mission that was designed to measure the radiation belt system, and thus provide high quality data (Mauk et al., 2013). For example, RBSP have excellent energy resolution to study the highly variable outer belt electron dynamics and instrumentation to monitor the local plasma waves that are critical for accelerating, precipitating and transporting the electrons. The two spacecraft had highly elliptical orbits spanning $L \sim 2$–6 with a low orbital inclination of $10°$ and an orbital period of about 9 hours. The spacecraft thus frequently sampled nearly equatorially mirroring particles ($\sim 90°$ pitch angles). Pitch angle resolved electron fluxes were measured by the Magnetic Electron Ion Spectrometer (MagEIS; Blake et al., 2013) at energies from 30 keV to 1.5 MeV and the Relativistic Electron Proton Telescope (REPT; Baker et al., 2013) at energies from 1.8 to 10 MeV of the Energetic Particle, Composition, and Thermal Plasma instrument suite (ECT; Spence et al., 2013). The local magnetic field was measured by the Electric and Magnetic Field Instrument Suite and Integrated Science (EMFISIS; Kletzing et al., 2013). Information about the magnetic field magnitude and particle pitch angles are required for calculating phase space density (see, e.g., Morley et al., 2013; Hartley & Denton, 2014). However, having only two spacecraft limits the temporal resolution in terms of spatial coverage, especially since the orbits were designed so that one probe trailed the other. Therefore, the Van Allen Probes cannot provide global data on the short timescales required to fully evaluate the radiation belt response to solar wind transients.

While the primary purpose of GPS satellites is to provide information for navigation, they can also provide useful data for space science (Morley et al., 2016, 2017). The main advantage is the large number of satellites that are able to provide broader spatial coverage and thus finer temporal resolution in terms of L-shell and magnetic local time. For example, Morley et al. (2016) showed that the data from 17 GPS satellites allow nearly continuous coverage of the outer belt at a timescale of only 20 minutes. The GPS satellites are on near-circular medium-Earth orbits, distributed on six orbital planes. They cover the outer radiation belt slightly further out than RBSP with $L \sim 4$–8 and have an orbital period of 12 hours. The nominal orbital inclination is $55°$, which limits the range of equatorial pitch angles of the observed populations. Electron counts are measured above about 120 keV by the Combined X-ray and Dosimeter (CXD; Tuszewski et al., 2004) and the counts can be converted to fluxes using a flux forward model (Morley et al., 2016). Morley et al. (2016) performed a cross-calibration of RBSP and GPS data, and showed that the flux measurements are generally within a factor of 2 from each other. The GPS instrumentation is also well inter-calibrated between GPS satellites. The primary drawbacks of utilising GPS data for radiation belt studies are that the particle measurements are not pitch angle resolved and the satellites do not have magnetometers. Therefore, a PAD model and a geomagnetic field model are required in order to calculate PSD and all three adiabatic invariants for GPS, whereas RBSP observed the directional fluxes and had measurements available to compute the first adiabatic invariant. A global geomagnetic field model is required for the second and third adiabatic invariants in any case since they depend on the global geometry of the field.

2.2 Flux Data and PSD Calculation

Electron fluxes are typically considered as a function of spatial location, energy and pitch angle (unless monitored by an omnidirectional instrument, such as onboard GPS satellites). Investigating changes in the flux shows how electrons in the outer belt respond to solar wind driving at different L-shells and energies (e.g., Turner et al., 2019; Kalliokoski et al., 2020). However, fluxes can be misleading as adiabatic processes (such as the Dst effect) can appear to cause losses or enhancements in the electron fluxes but do not permanently change the electron dynamics (Kim & Chan, 1997). Non-adiabatic changes evidencing true losses – precipitation to the atmosphere (e.g., Kennel & Petschek, 1966) or loss through the magnetopause (e.g., Turner et al., 2012) – or energisation – via wave-particle interactions (e.g., Chen et al., 2007) – are revealed by studying PSD, which is a quantity that remains constant under adiabatic processes. Calculating PSD includes conversion from location, energy and pitch angle to presenting the data in terms of the adiabatic invariants, μ, K and L^* (see, e.g., Green & Kivelson, 2004), which requires the use of a global geomagnetic field model. If PSD is calculated from GPS measurements, a PAD model is also required to convert the omnidirectional measurements into pitch-angle resolved data. PSD is a more powerful tool for analysing electron acceleration, transport and loss mechanisms in the outer radiation belt in response to magnetospheric disturbances (e.g., Chen et al., 2007; Turner et al., 2012; Shprits et al., 2017; Kalliokoski et al., 2022). Below, we have described how the flux and PSD were acquired and calculated from RBSP and GPS data.

Van Allen Probes electron data is available on the ECT website (`https://rbsp-ect.newmexicoconsortium.org/science/DataDirectories.php`, last access: 30 May 2022). The level-2 spin-averaged differential electron fluxes were used when comparing with the omnidirectional GPS fluxes. For calculating PSD, we used the level-3 pitch angle resolved fluxes, as well as the magnetic field magnitude measurements from EMFISIS which are available on the EMFISIS website (`https://emfisis.physics.uiowa.edu/data/index`, last access: 30 May 2022). The magnetic ephemeris data, which are also available on the ECT website, were used to acquire the second and third adiabatic invariants K and L^* calculated from the Tsyganenko and Sitnov (2005) TS04D geomagnetic field model. PSD was calculated from MagEIS data at lower energies (10s keV to 1 MeV) and REPT data at higher energies ($>$ 1 MeV) as described in Kalliokoski et al. (2022), where flux was converted to PSD following the formulation in Chen et al. (2005). No fits to pitch angle or energy distributions were employed in this method, and interpolations were performed to get the K and L^* corresponding to the equatorial pitch angles mapped from observations and to increase the energy resolution by adding two artificial energy channels in between the instrumental channels. We note that when investigating RBSP PSD, μ and K were calculated over ranges of the first and second invariants, instead of being fixed to a single value, which allows for a better resolution in PSD (see Kalliokoski et al., 2022). We consider near-equatorially mirroring electrons with $K \leq 0.05\ R_E \mathrm{G}^{1/2}$ and for μ, the range is 6.7% of the central value (e.g., $\mu = (3000 \pm 100)$ MeV/G).

CXD electron data from the GPS constellation are publicly available and archived by the National Oceanic and Atmospheric Administration's National Centers for Environmental Information (`https://www.ngdc.noaa.gov/stp/space-weather/satellite-data/satellite-systems/gps/`, last access: 30 May 2022). The GPS satellites are identified by their satellite vehicle number (SVN) and in this study, we used GPS satellites from ns53 to ns73. Data from these satellites are available from between 2001–2016 (start date varies between satellites) until the present. GPS measured electron counts were converted to omnidirectional fluxes by a flux forward model which is a combination of three relativistic Maxwellian functions and one Gaussian function (for details, see Morley et al., 2014; Morley et al., 2016). The fit parameters are included in the GPS data product. The fitting can be used to calculate the omnidirectional flux at any given energy from 140 keV to 4 MeV where the quality of measurements is good (Morley et al., 2016). Due to intermittent noise, the fits from ns60 can be unreliable, so we have excluded it from our study. Data from other satellites were filtered based on the goodness of fit following Smirnov et al. (2020): the measured counts were compared to the modeled counts from the fit in the five lowest energy channels, and the data was discarded if the discrepancy was too high. This approach is conservative and tends to exclude particularly low flux data. This manifests as a removal of data at high L in addition to the removal of bad fits. We note that suspect data indicated by the "`dropped_data`" flag was also discarded.

PSD was calculated from the GPS data following the steps outlined in, e.g., Hartley and Denton (2014). Briefly, this involves determining the energy and pitch angle from given μ and K values, obtaining the measured flux at that energy and pitch angle, calculating the corresponding L^*, and dividing the flux by momentum squared to obtain the PSD as a function of the adiabatic invariants. PSD calculation from GPS data requires fitting with models, which means we can choose a constant value for μ and K, in contrast to RBSP. First, using the LANLGeoMag library (Henderson et al., 2018) with the satellite position as input, we computed the equatorial pitch angles and L^* values corresponding to the chosen K as well as the local and equatorial magnetic field magnitude. The TS04D global geomagnetic field model was used. Second, the electron energy corresponding to the chosen μ was determined using the modeled variables, and the omnidirectional flux at this energy was derived from the flux forward model. Third, a PAD model, describing the angular distribution of electron flux, was employed to acquire the directional flux, which was converted to PSD as given in Chen et al. (2005).

We used the empirical relativistic electron pitch angle distribution (REPAD) model (Chen et al., 2014), constructed from fitting Legendre polynomials to observed PADs, which can describe a wide variety of observed PAD shapes (e.g., pancake, butterfly). Along with parameters from the magnetic field model, it takes the AE index as input, which we obtained from the OMNI database through the NASA Goddard Space Flight Center Coordinated Data Analysis Web at 1-minute cadence (`https://cdaweb.gsfc.nasa.gov/index.html/`, last access: 30 May 2022). The equatorial PAD from the model was normalized by the omnidirectional flux measurement by GPS. The model then gave the directional flux at any equatorial pitch angle corresponding to the chosen K. Since the GPS can be at high latitudes away from the equator, the range of equatorial pitch angles the satellite can measure may become small. This approach uses REPAD to define the equatorial PAD and thus the directional fluxes at equatorial pitch angles not measurable at GPS can be considered an extrapolation from data. The uncertainty of the directional differential fluxes at near-equatorially mirroring pitch angles is therefore larger when CXD measures only a small fraction of the equatorial pitch angle space. To mitigate this uncertainty, we computed the ratio of the portion of the PAD that GPS measures and the full distribution, and discarded data where this ratio was less than 10%. Again, data is most notably removed at high L^*, limiting the coverage of GPS PSD. The calculation of the normalization and the aforementioned ratio is presented in more detail in Appendix A.

To illustrate how the two data sets compare, we show a sheath event that impacted the magnetosphere on 15 February 2014 in Figure 1. This event resulted in overall loss that was seen in both fluxes and PSD, and there was also a brief enhancement during the leading part of the sheath. The top row shows RBSP data and GPS data is shown on the bottom row, with fluxes shown on the left and PSD on the right. The data is binned 30 minutes in time and 0.1 in L-shell for fluxes or L^* for PSD. For fluxes, the dark grey areas indicate bins with at least one satellite present but where the data is either below the instrument level or low quality. For RBSP PSD, the dark grey areas similarly indicate that a satellite was present but PSD could not be computed in the given μ and K ranges. For GPS PSD, the dark grey color was chosen to show the regions where the PAD model was uncertain (i.e., PAD ratio below 10%).

Figure 1 contrasts the spatial and temporal coverage of the two constellations, and we can immediately see the differences in the data density of RBSP and GPS. GPS provide nearly continuous coverage at a 30-minute timescale while RBSP data have gaps of multiple hours at a given L-shell or L^*. This highlights how GPS data can provide information further out in the belt than RBSP and how GPS provide data at higher time resolution, though high quality GPS PSD can be restricted to about $L^* \sim 4$–5. The GPS data can therefore be used to analyse the localised spatial and temporal dynamics of the outer belt electrons in a capacity not possible with the RBSP. This capacity

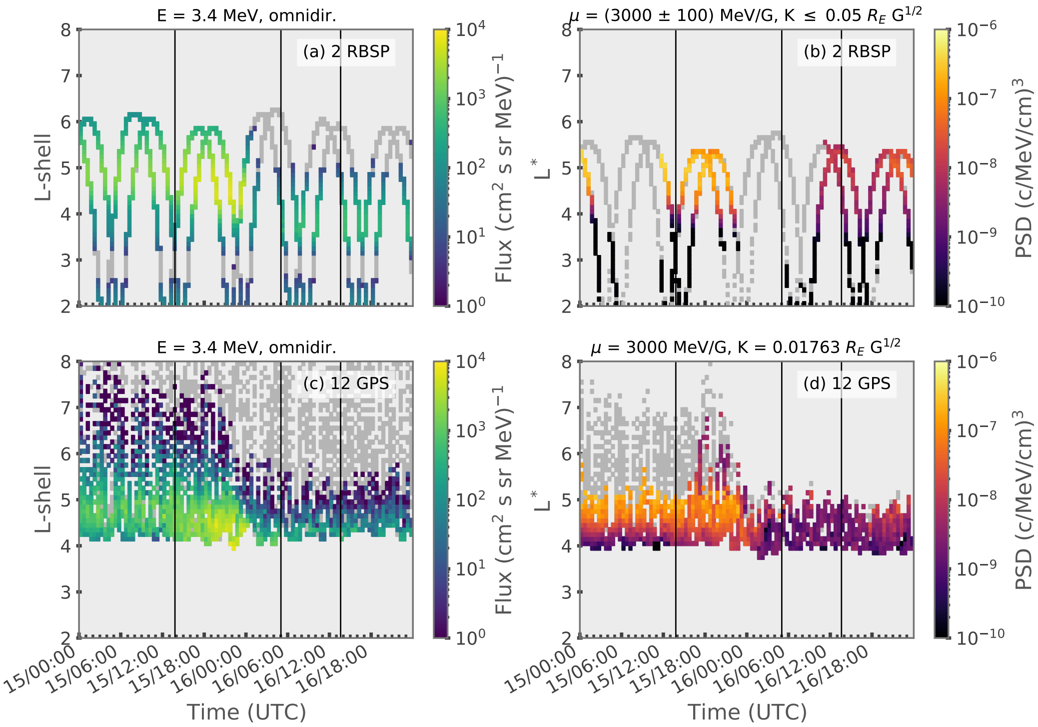

Figure 1. Comparison of data from two RBSP (top) and 12 GPS (bottom) satellites during a sheath event on 15 February 2014. Electron fluxes at 3.4 MeV are shown on the left and PSD at $\mu = 3000$ MeV/G with a K value/range corresponding to near-equatorial electrons are shown on the right. The data are binned 30 minutes in time and 0.1 in L-shell or L^*. For fluxes and RBSP PSD, the dark grey areas show when the satellites were present but the data are deemed poor quality or PSD cannot be computed. For GPS PSD, the dark grey areas indicate poor quality PAD fitting. The black vertical lines indicate the shock, ejecta leading edge and ejecta trailing edge with the sheath region between the two first lines.

provided by GPS satellites is particularly important when evaluating the rapid changes caused by ICME-driven sheaths or other solar wind transients.

We analyse the outer radiation belt electron response with the higher data density GPS data in comparison with the results from RBSP in the next two sections considering both the electron fluxes and PSD.

3 Flux Response

This section presents the reproduction of the study by Kalliokoski et al. (2020) with the GPS data and discusses the differences in the results obtained using the RBSP and GPS data sets. The comparison is first done with similar 6-hour averaging for both data sets and then repeated for the GPS data with 30 minute averaging to explore the effect of capturing the more immediate sheath response.

In Kalliokoski et al. (2020), the authors studied the overall response of the outer radiation belt electron fluxes to the impact of ICME-driven sheath regions using RBSP measurements over a broad energy range (10s keV to several MeV). The study included 37 sheaths in 2012–2018. The change in electron fluxes was parameterized with the response parameter (R) based on the methodology of earlier response studies (e.g., Reeves et al., 2003; Turner et al., 2015, 2019). The flux was averaged before and after the sheath region and the response parameter was defined as the ratio of the post-sheath to pre-sheath flux averages for each considered energy and L-shell. A 6-hour averaging period was selected as it was the shortest time period that still ensured sufficient L-shell coverage by RBSP. The response parameter was used to divide the outer belt response into three categories: enhancement ($R > 2$), depletion ($R < 0.5$) and no significant change ($0.5 \leq R \leq 2$).

The energy and L-shell dependencies of the outer belt response as calculated from the RBSP data are shown in the top panels of Figure 2 (reproduced from Figure 6 in Kalliokoski et al., 2020). The data are binned 0.1 in L-shell and according to the MagEIS and REPT energy channels (note that the channels have variable widths and the energies covered are not continuous). Each column shows a different type of response, with the color scale showing the percentage of sheath events causing each response in each of the energy-L bins. The percentage value was calculated by dividing the number of events causing, for example, enhancement in a given energy-L bin by the number of events where there were data to compute the response parameter in that bin. This number of events where data was available is shown in the right-hand column. We see that the response parameter can be calculated from RBSP data throughout the outer belt from almost all events. At $L \sim 3$ and at about 1 MeV energies, the lower RBSP data availability is due to low quality MagEIS data.

The 6-hour averaged results reproduced using the GPS data are shown in the middle panels of Figure 2 in the same format as the response from RBSP data. For each event, fluxes at the same energies as the RBSP energy channels (in the range from 140 keV to 4 MeV) were derived from all GPS satellites with the measurements available. The response parameter could be computed from more than half of the events at about $L =$ 4–6 (GPS data availability is the same for all energies due to the flux forward model). The data are more sparse further out since GPS spend less time there and the fitting procedures do not perform as well at high L-shells leading to the goodness of fit filtering further reducing the data.

Visual comparison of the 6-hour averaged responses computed from the RBSP and GPS data in Figure 2 (top and middle panels) indicates that GPS reproduces the overall features of the results in all three categories at $L =$ 4–6. The GPS response shows very similar energy and L-shell dependencies: (1) enhancement is common at 100s keV and its likelihood increases for higher energies ($>$ 400 keV) with decreasing L-shell; (2) depletion is common at $>$ 1 MeV and its likelihood increases at lower energies (100s keV) with increasing L-shell; (3) between enhancement at low energies and depletion at high energies, there is a band at $L =$ 4–6 where no significant changes (no flux increase or decrease by over a factor of 2) are typical. There are only subtle differences. Slightly more sheaths lead to enhancement at higher L-shells and to depletion at higher energies for the RBSP than for the GPS. The no change response from the GPS is slightly more common at higher energies as compared to the RBSP no change response.

The GPS data allows for calculating the response also at L-shells above the maximum sampled L of RBSP, but our current data filtering to ensure reliable results is very conservative and leads to low data availability at high L, with fewer than 10 events included. Therefore, the response shown from GPS at $L > 6$ should be carefully considered with the number of available events in mind. The percentage value of response shown in the panels can have very low or high values (appearing as, e.g., bright yellow spots) due to the limited number of events at $L > 6$. The overall trend at $L > 6$ continues similarly as in lower L-shells with enhancement at low energies and depletion at high energies.

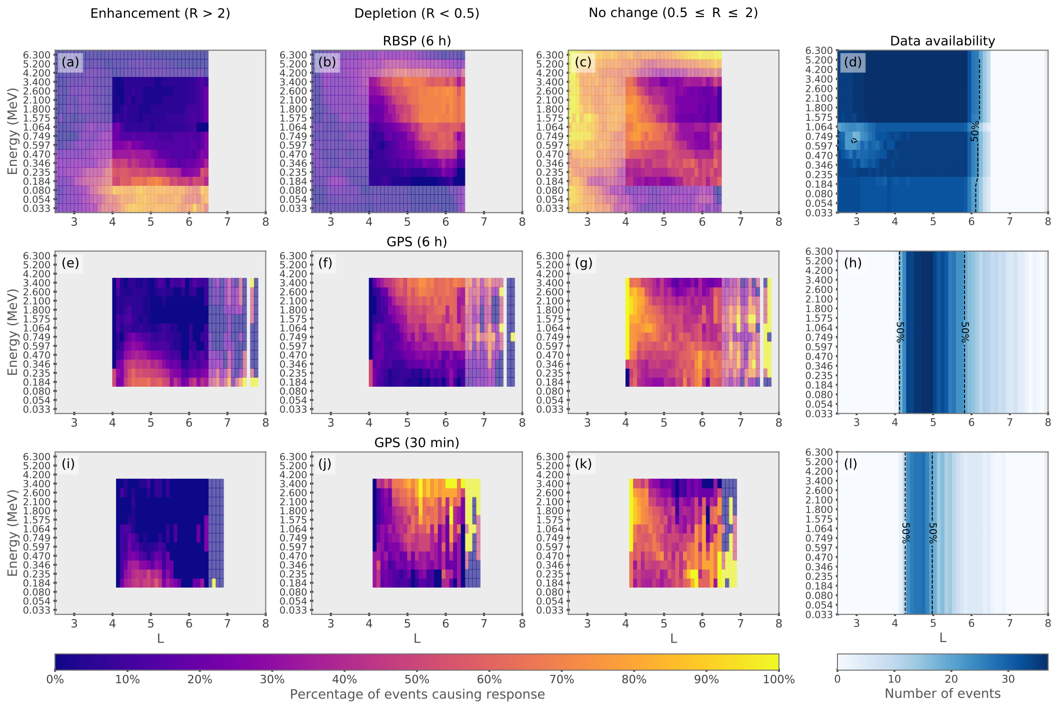

Figure 2. Comparison of outer belt electron flux response calculated from 6-hour averaged RBSP data (top) and 6-hour and 30-minute averaged GPS data (middle and bottom). Panels on the first three columns show the percentage of sheath events causing enhancement, depletion, or no change at each energy and L-shell. Note that the sum of percentages from all three categories in any given energy-L bin is 100%. RBSP response below the minimum sampled L of GPS and GPS response above the maximum sampled L of RBSP are shown faded out to highlight the area in the heart of the outer belt where there are data from both missions. Similarly, response at energies which GPS do not measure are shown faded out for RBSP. The data availability panels on the right show the number of sheath events where the response parameter could be computed at each energy and L-shell. The dashed contours indicate the area where data are available from more than half of the events.

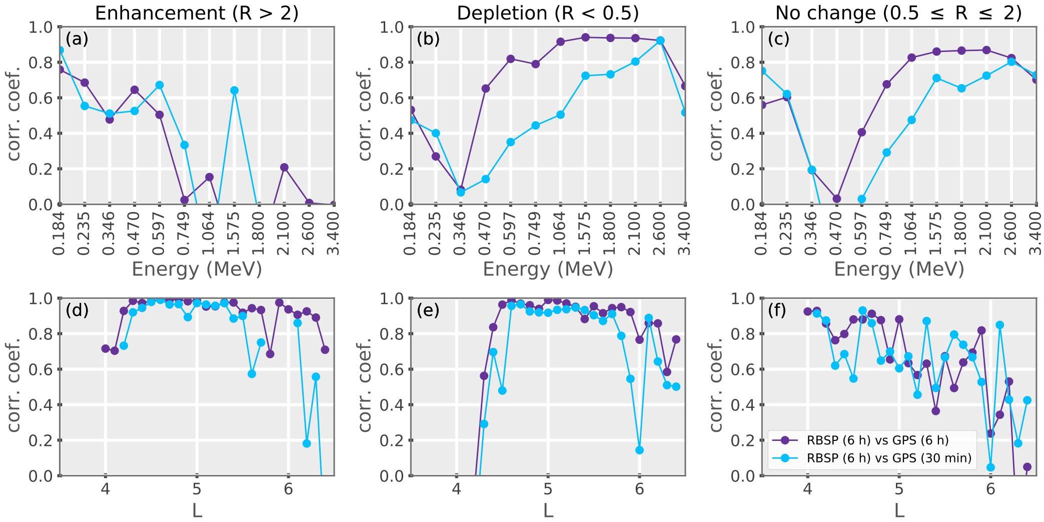

Figure 3. Pearson correlation coefficients calculated from data at each energy (top row) and L-shell bin (bottom row) for each response category, quantifying the agreement of RBSP and GPS flux response shown in Fig. 2. Purple lines show correlation between 6-hour averaged responses and blue lines between 6-hour RBSP and 30-minute GPS responses.

We give a more quantitative confirmation of the correspondence in responses from RBSP and GPS by calculating the correlation between the response data in each category. The correlation was calculated both at each energy bin and each L-shell bin in the range where the data is available from both missions (from 140 keV to 4 MeV and $L = 4$–6.4). The correlation coefficients are shown in Figure 3 for each energy bin (top) and for each L-shell bin (bottom) with the purple lines for the 6-hour responses. The correlation computed at each L-shell is excellent and shows that the energy dependence of the responses from both missions is virtually identical. The correlation drops at the lowest and highest L, most notably for no change response with increasing L. The drop is due to the GPS data availability decreasing at these L-shells which produces more abrupt features in the response percentage values in contrast to RBSP, as well as the difference in the energy extent of the no change responses noted above. The L-shell dependency, shown by the correlation coefficients computed at each energy, is also mostly well correlated, but the correlation is low at some energies. For example, both depletion and no change display a drop to no correlation at about 300–500 keV, which indicate the largest discrepancies in the L-shell extent of the responses mentioned above. Correlation between enhancement responses is low at high energies as the likelihood of enhancement is close to zero from both RBSP and GPS at these energies. When the response was computed including only the subset of sheath events that had both RBSP and GPS data available (determined per bin), we again found a low correlation at similar energies and L-shells (though the correlation is overall higher; not shown). This indicates that the missions resolve slightly different dependencies of the response.

We repeated the response analysis described above for the GPS data but averaging the fluxes over 30 minutes instead of 6 hours. RBSP cannot provide data at such a short timescale, so this study was enabled by employing data from multiple GPS satellites that provide better temporal resolution in the heart of the outer belt. The results are presented in the bottom row of Figure 2. The data are now largely limited to $L =$ 4–5, as this is the L range where the GPS data was available both 30 minutes before and after the sheath for the majority of the investigated events. Nevertheless, visual comparison to the RBSP response (Figure 2 top and bottom panels) and the correlation (blue lines in Figure 3) show that similar energy and L-shell dependencies are reproduced at the shorter timescale. This confirms that the observed changes in electron fluxes reported in Kalliokoski et al. (2020) (and reproduced by the 6-hour averaged GPS data) were caused specifically by the sheath with no significant contribution from processes during the ejecta. However, the short timescale response reveals some differences to the 6-hour response. We see that the 30-minute averaged GPS response shows enhancement being less common and depletion being more common than for the 6-hour averaged responses (especially evident when comparing responses for the same subset of sheath events; not shown). This implies that some of the initial recovery of electron fluxes during the ejecta have been included in the 6-hour response.

We also calculated the response from the GPS data when the sheath events were divided to geoeffective and nongeoeffective events (Figure S1), similar to what was done in Kalliokoski et al. (2020). A geoeffective event was identified by a drop in the *SYM-H* geomagnetic activity index below −30 nT during the sheath or 2 hours after it (as the ring current takes time to build up). This analysis similarly reproduced the energy and L-shell dependencies of the response from RBSP as presented in Kalliokoski et al. (2020). Briefly, both enhancement and depletion are more common during geoeffective events. While less common, significant changes occur also during nongeoeffective sheaths where enhancement extends only up to $\sim$ 300 keV and depletion is likely above $L \sim 5$ except for only the highest energies which deplete also at lower L. For geoeffective sheaths, enhancement extends up to $\sim$ 700 keV at low L and depletion is observed throughout $L = 4$–6.

4 Phase Space Density Response

The flux response shows how the electron content in the outer belt changes due to sheaths and how variations depend on energy and L-shell. However, only PSD can reveal the irreversible acceleration and loss of electrons. The methods to calculate PSD from RBSP and GPS data were presented in Section 2.2. Since PSD is expressed in terms of the adiabatic invariants, we consider next the μ and L^* dependency of the response instead of energy and L-shell. Furthermore, while we considered omnidirectional fluxes, we now focus on the near-equatorially mirroring electrons and have chosen the K value (or range) accordingly. GPS PSD was computed for $K = 0.02\ R_E\mathrm{G}^{1/2}$ and RBSP PSD for $K \leq 0.05\ R_E\mathrm{G}^{1/2}$. PSD was computed for μ values from 100 to 5000 MeV/G at 100 MeV/G increments, and the response was binned 0.1 in L^*.

Our key focus here is to investigate the PSD response to geoeffective and nongeoeffective sheath events, which show interesting differences in their electron dynamics. To briefly discuss the results for all events, they are shown combined for 6-hour averaged RBSP PSD response and 6-hour and 30-minute averaged GPS PSD responses in Figure S2 in Supplementary materials. The results between the RBSP and GPS data are very similar. Correlation is lower than for the flux response, but is still quite high (Figure S3). PSD changes are particularly small at lower μ and L^*. In more than 30% of the cases, a broad range of electron populations are depleted at $L^* > 4.5$. Electrons tend to be accelerated only at very low μ ($<$ 500 MeV/G).

The PSD response for 17 geoeffective sheaths (top) and 20 nongeoeffective sheaths (bottom) are shown in Figure 4. We see that the data availability from RBSP is similar between the two event types with data from slightly more than half of the events at $L^* < 5$. GPS data is available from almost all nongeoeffective sheaths at $L^* = 4$–5 while good data coverage is more limited in L^* during geoeffective sheaths. We note that the band of lower RBSP data availability at $\mu < 2000$ MeV/G is related to PSD being calculated predominantly from REPT and MagEIS data above and below this band, respectively. Again, RBSP and GPS responses show overall very similar characteristics.

The correlation coefficients shown in Figure 5 reveal also again quite large variability from negligible correlation to strong correlation, but in general correlation with both μ and L^* is moderate or strong. There are no obvious trends in correlation found as a function of μ or L^*, but the majority of strong correlation are found for mid-range μ between 1500–3500 MeV/G.

The distinct difference between geoeffective and nongeoeffective sheaths is that only geoeffective sheaths accelerate electrons efficiently, causing an enhancing response in $>$ 30% of the events throughout the heart of the outer belt ($L^* = 4$–5) at all μ values. Acceleration is more frequent ($> 50\%$ of the events) at low μ (< 500 MeV/G). The 6-hour GPS response indicates local acceleration at $L^* \sim 4$ at higher μ values during a larger number of sheaths than the 30-minute averaged response. This is only partly explained by the higher data availability between 6-hour and 30-minute GPS responses, suggesting that the extra acceleration in the 6-hour response is related to the ejecta. In addition, due to better data availability, the GPS captures more sheaths, and hence its statistics are expected to be more reliable than for RBSP. However, it should be noted that good data coverage is limited to a very narrow L^* range for geoeffective events, $L^* =$ 4–4.5. In this L^* range, in 6-hour GPS data about 30–60% of the events lead to acceleration at a wide range of μ values, while for RBSP the fraction of enhancing events in the same L^* range is only about 20–30%. The GPS response also indicates more acceleration even when the analysis is repeated using only the same subset of the sheath events for GPS and RBSP (not shown). For nongeoeffective sheaths, acceleration is observed only during very few events at $L^* = 4$–5.5 for the lowest μ.

Losses are observed frequently during both geoffective and nongeoeffective sheaths, and in particular at the largest L^* captured where typically over half of the events cause depletion for all μ except the few lower bins. The two types of sheaths have some differences in the extent and μ dependence of depletion. During geoeffective sheaths, losses typically extend (for $> 30\%$ of the events) to lower L^* than for nongeoeffective events, $L^* \sim 4$ and $L^* \sim 4.5$, respectively. However, the 30-minute GPS response shows losses extending down to $L^* \sim 4$ at the highest μ values even during nongeoeffective events. For nongeoeffective sheaths, loss is also more likely (in $> 50\%$ of the events) at high μ (> 2000 MeV/G) where the likelihood does not change much with L^* (above $L^* = 4.5$). At lower μ values, loss is restricted to above $L^* \sim 5$. For the 30-minute averaged response, losses are also more frequent, which is clearly present also when the response is computed only from the same subset of the nongeoeffective sheath events (not shown). On the other hand, losses are observed about as frequently for 6-hour and 30-minute responses at all μ values during geoeffective sheaths. Losses seem to become more common with increasing L^* but the data availability also decreases with increasing L^* for both satellite missions, so no strong conclusions can be made regarding the L^* dependency or if depletion is more common during geoeffective than nongeoeffective sheaths. We note that the RBSP response for geoeffective sheaths has only a few depleting events for the lower μ values (< 1500 MeV/G). Though, the difference in RBSP and GPS responses in this μ range is smaller when the analysis is repeated using only the same subset of the sheath events (not shown). Finally, the no-change response is much more common during nongeoeffective sheaths. There is a trend of increased likelihood of no changes in PSD at low μ and low L^* which is visible in both cases but is more distinct in the GPS response and during nongeoeffective sheaths.

5 Discussion

This paper has investigated the usage of the recently released GPS constellation energetic particle data set for investigating the response and dynamics of radiation belt high-energy electrons. We first reproduced the analysis from Kalliokoski et al. (2020), who used RBSP data, with the energetic charged particle data from GPS. We then removed adiabatic effects, including those likely to arise from storm-time ring current build-

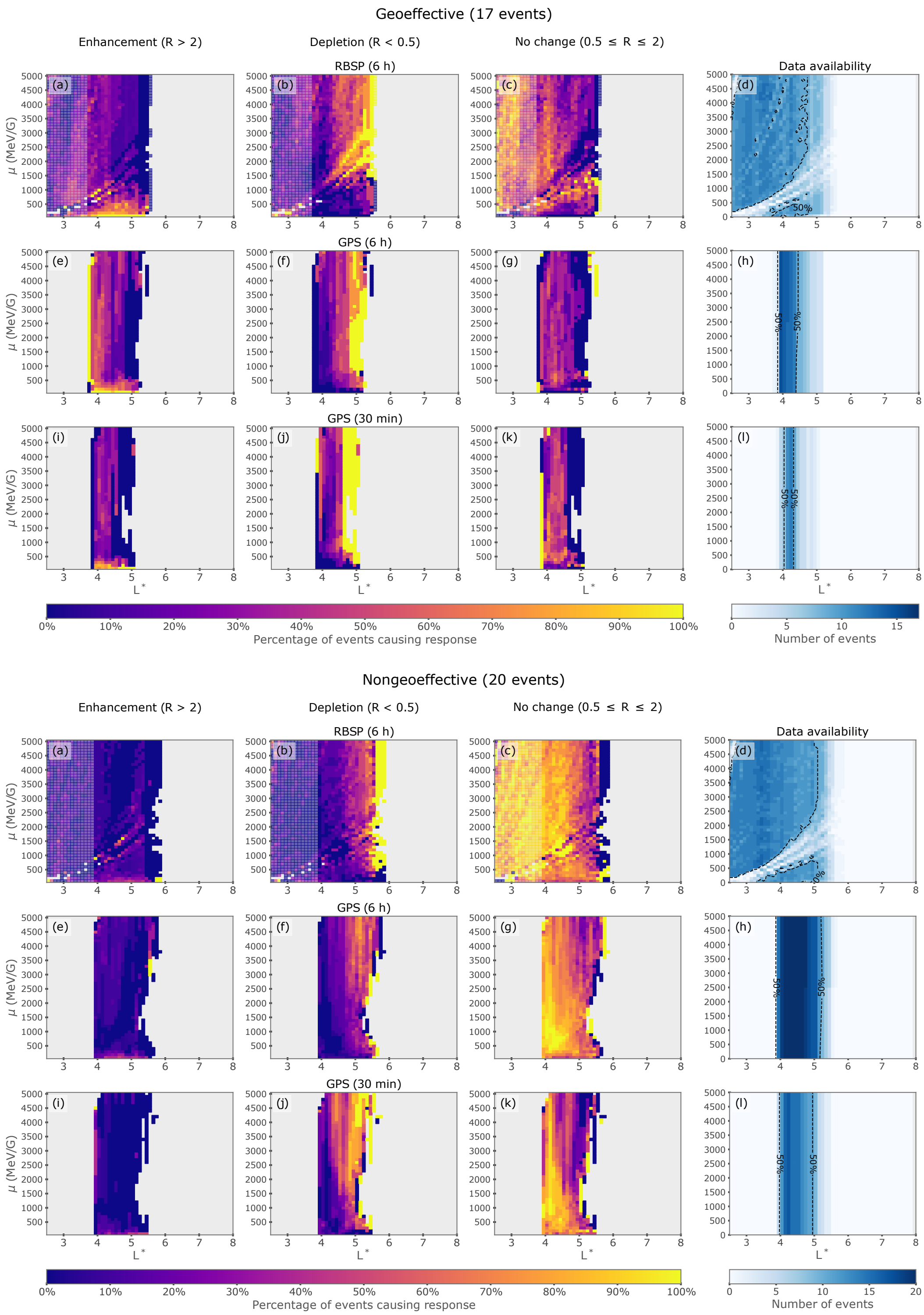

Figure 4. Comparison of outer belt electron PSD response for geoeffective (top) and non-geoeffective (bottom) sheath events in the same format as in Fig. 2. Response calculated from (a–c) 6-hour averaged RBSP data, (e–g) 6-hour averaged GPS data and (i–k) 30-minute averaged GPS data is shown for both set of events. Panels on the first three columns show the percentage of sheath events causing enhancement, depletion, or no change at each first and third adiabatic invariant, μ and L^*. The second adiabatic invariant is $K \leq 0.05\ R_E\mathrm{G}^{1/2}$ for RBSP PSD and $K = 0.02\ R_E\mathrm{G}^{1/2}$ for GPS PSD. Note that for RBSP PSD, μ values include a 6.7% range from the shown central value. RBSP response below the minimum sampled L^* of GPS is shown faded out to highlight the L^* range where there are data from both missions. The data availability panels on the right show the number of sheath events where the response parameter could be computed at each μ and L^*. The dashed contours indicate the area where data are available from more than half of the events.

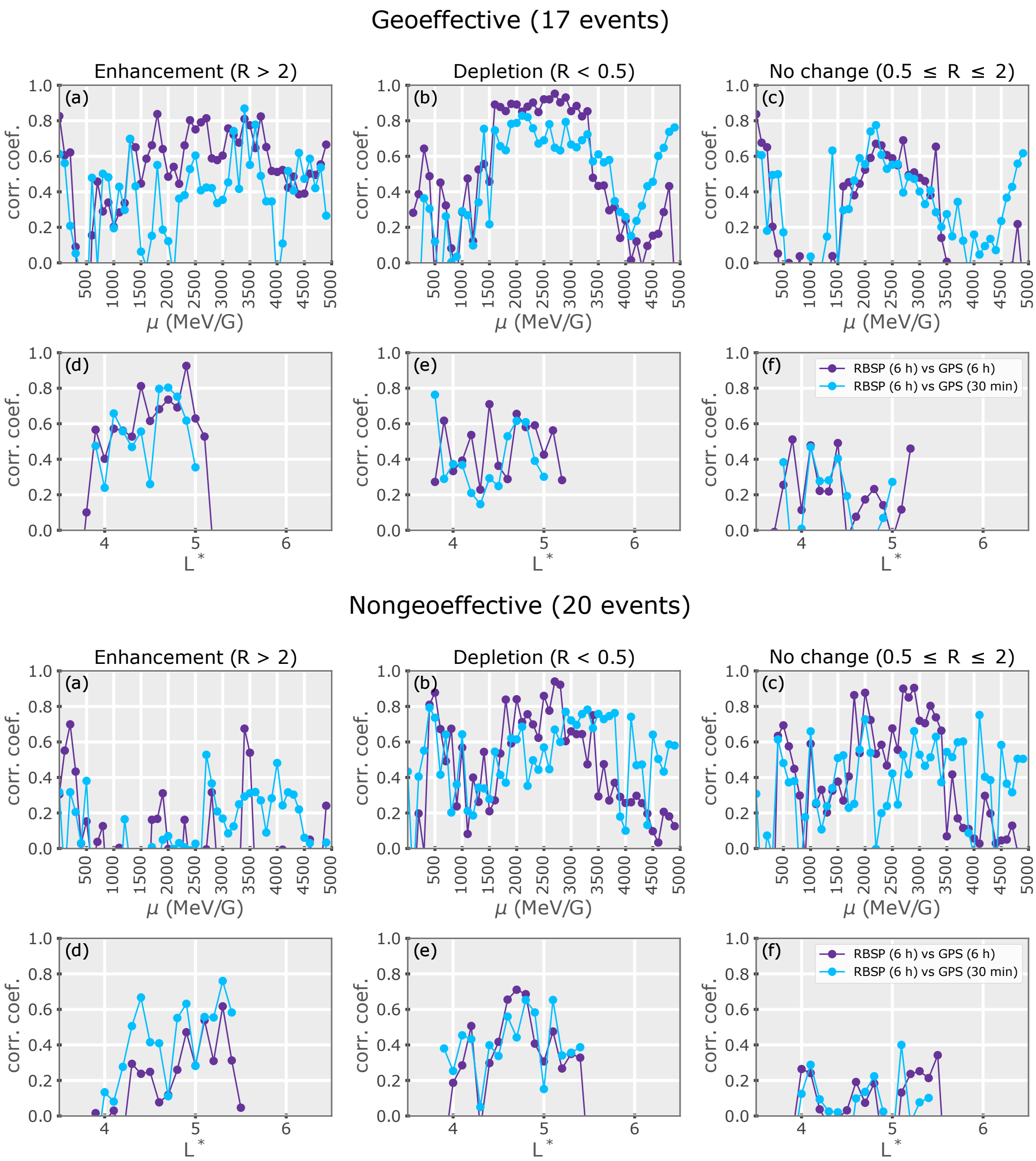

Figure 5. Pearson correlation coefficients for responses during geoeffective (top) and nongeoeffective (bottom) sheath events. Correlation is shown for each (a–c) μ value and (d–f) L^* bin for each response category, quantifying the agreement of RBSP and GPS PSD response shown in Fig. 4.

up, by performing a similar analysis using PSD in adiabatic coordinates with both data sets. The study investigated the response of the outer belt to 37 ICME-driven sheath regions. The determination of the response parameter (i.e., parameter comparing the fluxes/PSD before and after the sheath, in other words, the overall response to the sheath) is limited to 6 hours for RBSP data as it consist of two spacecraft only. With GPS, the response parameter can be calculated with much higher temporal resolution of 30 minutes. We compared the results using the response parameter calculated with 6-hour averaging for both RBSP and GPS, and for GPS also using 30-minute averaging.

The 6-hour averaged flux response calculated from GPS data was very similar to the response calculated from the 6-hour averaged RBSP data. The 30-minute averaged GPS response confirmed that the overall changes in fluxes as reported in Kalliokoski et al. (2020) are due to the sheath region and not the early ejecta. In addition, they revealed some subtle yet important differences. Enhancement is slightly less frequent and depletion more likely on fast time scales of 30 minutes after the sheath rather than 6 hours after it, indicating that a portion of the depletion is quickly recovered after the sheath. The higher likelihood for loss is also shown by Turner et al. (2019) who reported the response for isolated sheaths (i.e., no following ejecta to drive the recovery). Since depletion becomes less frequent during the ejecta at high energies (> 500 keV) and the number of enhancing events increases at lower energies (< 500 keV), such flux recovery affects the overall outer belt electron populations. This can likely be explained by the longer time period allowing for more substorm injections and subsequent acceleration to higher energies, as well as by the lack of conditions leading to effective losses during the ejecta. As shown by the statistical analysis of Kalliokoski et al. (2020), the geomagnetic disturbances are stronger during the ejecta, which causes elevated substorm activity, while in the sheath the combination of relatively high dynamic pressure compressing the magnetopause and enhanced wave activity provide favorable conditions for electron losses through the magnetopause (i.e., magnetopause shadowing; Turner et al., 2012) and scattering the electrons away from the belts. During the ejecta, in turn, the magnetopause starts to move further out and wave activity is relatively less intense (e.g., Hietala et al., 2014; Kilpua, Fontaine, et al., 2019; Kalliokoski et al., 2020), diminishing magnetopause shadowing losses and precipitation.

To remove adiabatic effects, we investigated the PSD response. This extends the analysis of Kalliokoski et al. (2020) who used RBSP data to examine the response to sheaths in radiation belt flux. The shape of PSD radial profiles can be used to identify the acceleration, transport and loss processes governing the electron dynamics (e.g., Chen et al., 2007; Turner et al., 2012; Shprits et al., 2017) but the response parameter studied in this paper hides such details during the sheath. Nevertheless, the μ and L^* dependencies of the PSD response can shed light on the energisation and loss mechanisms.

During geoeffective sheaths, enhancements are seen near $L^* \sim 4$ indicating local acceleration. Geoeffective sheaths are typically associated with strong substorm activity (e.g., Pulkkinen et al., 2007; Kalliokoski et al., 2020), which in turn excites chorus waves that can efficiently accelerate electrons to > 1 MeV energies (Miyoshi et al., 2013; Jaynes et al., 2015). Comparing the GPS response over the two timescales, acceleration is more common over 6 hours than 30 minutes. Since geoeffective sheaths are also associated with geoeffective ejecta (Kalliokoski et al., 2020), the geomagnetic activity started during the sheath is expected to continue, and therefore also the excitation of chorus waves and progressive acceleration of electrons to higher energies persist during the early ejecta. Losses are observed to be common at high L^* at a variety of μ values during geoeffective sheaths, indicating loss at the magnetopause. Outward radial diffusion driven by ultra-low frequency waves, whose activity is elevated during sheaths and especially during geoeffective ones as shown by Kalliokoski et al. (2020), can further transport electrons to the magnetopause. This tandem process of inward magnetopause incursion and outward transport is also associated with enhancements at lower L^* due to concurrent inward radial diffusion (Turner & Ukhorskiy, 2020).

Losses in PSD are common at high L^* indicating magnetopause shadowing losses also during nongeoeffective sheaths. The 30-minute response shows losses to be even more frequent which points, as also discussed above, to electrons being energised during the ejecta to about pre-event levels especially at $L^* = 4$–4.5. For nongeoeffective sheaths, the losses penetrate as deep into the outer belt as during geoeffective events only at high μ values with the 30-minute response. The magnetopause erosion is however not as efficient for nongeoeffective sheaths as for geoeffective sheaths (Kalliokoski et al., 2020), which could imply that in the inner parts of the outer belt scattering by wave-particle interactions has a key role in causing losses. Electromagnetic ion cyclotron (EMIC) waves can scatter multi-MeV electrons rapidly (Aseev et al., 2017; Shprits et al., 2017; Kurita et al., 2018). This scattering loss can also contribute to losses during geoeffective sheaths during which EMIC wave activity is more elevated (Kalliokoski et al., 2020). Conversely, our results clearly demonstrate that nongeoeffective sheaths do not produce favorable conditions for electron acceleration. Enhancements in fluxes (seen in Figure S1) are therefore due to adiabatic processes. During nongeoeffective sheaths, the ring current is not enhanced like during the main phase of a geomagnetic storm. Instead, the SYM-H index tends to increase (Kalliokoski et al., 2020), indicating a weakened ring current which, in turn, causes the equatorial geomagnetic field to strengthen. Electrons move inward to conserve the third adiabatic invariant and the fluxes increase. This can be described as the "opposite Dst effect". We note however that the flux response presented here was computed from the omnidirectional fluxes, whereas the PSD response focused on the near-equatorially mirroring electrons. Using the pitch angle resolved RBSP flux data, we computed the response of 90° pitch angle electrons (not shown) which is very similar to the omnidirectional flux response shown for nongeoeffective sheaths in Figure S1. Therefore, the adiabatic flux enhancements occur also for the near-equatorially mirroring electrons sampled by our PSD.

6 Conclusions

To summarize, ICME-driven sheath regions cause significant changes in outer belt electron populations with distinct differences between geoeffective and nongeoeffective sheaths. The irreversible energisation and loss are revealed by phase space density analysis in contrast to electron fluxes which include changes due to adiabatic processes. Overall, sheaths are important drivers of outer belt electron loss, while geoeffective sheaths can also cause efficient acceleration. Enhancements in electron flux during nongeoeffective sheaths are adiabatic, caused by the "opposite Dst effect". By considering the immediate changes in outer belt electrons after the impact of the sheath, it is confirmed that the observed variation is caused specifically by the sheath. The response over longer time periods of a few hours underestimates the sheath-driven loss as electrons recover during the early ejecta.

We showed that GPS data reproduces the results from analysis performed with RBSP data, confirming the good inter-calibration between these missions. In addition, this study highlights that synergy of GPS with RBSP establishes compelling possibilities for studies combining the data sets, with the denser GPS data being able to fill in the gaps in RBSP observations with its spatially better temporal resolution as well as reaching higher L-shells. The time the GPS satellites spend at higher L-shells ($L > 6$) is however clearly less than in the heart of the outer belt, but for case and statistical studies of solar wind structures that are more frequent than sheaths (e.g., slow–fast stream interaction regions), combined RBSP and GPS data can provide information of the outer belt covering L from 2.5 to 8. This could better reveal, for example, the peaks and dips in electron fluxes and PSD, and the associated acceleration and loss mechanisms that could be missed or misinterpreted with only the RBSP data (Boyd et al., 2018; Olifer et al., 2021; Turner et al., 2021). GPS measurements also provide a continuation of radiation belt monitoring in the post-RBSP era.

Future work is needed to expose the local spatial effects and timescales of changes in PSD in individual sheath events in more detail, as the response parameter approach does not take into account the details of the changes during the sheath. Such studies will allow comparisons of the timescales of changes to the timescales of known acceleration and loss processes (e.g., driven by wave-particle interactions with specific wave modes). High density GPS data are reliable tools that can be used to perform such studies.

Appendix A PAD Model Normalization

We present the equations for the normalization of the PAD model and calculating the parameter to determine goodness of fit. We follow Hess (1968, p. 65) and the GPS convention of defining the omnidirectional flux as per steradian (i.e., adding a $1/4\pi$ factor). The omnidirectional flux measured locally by a GPS satellite can be expressed by the integral of directional flux over the full solid angle

$$J(E) = \frac{1}{4\pi}\int\int j(E,\alpha)d\Omega = \int_0^{\pi/2} j(E,\alpha)\sin(\alpha)d\alpha \tag{A1}$$

where we have assumed that the directional fluxes are gyrotropic and that the distribution is symmetric in pitch angle. According to Liouville's theorem, the local and equatorial directional fluxes should match. Thus,

$$j(E,\alpha) = j(E,\alpha_{eq}) \tag{A2}$$

where α_{eq} is the equatorial pitch angle corresponding to the local pitch angle α based on the conservation of the first adiabatic invariant.

Since GPS satellites do not measure the pitch angle resolved fluxes, a PAD model is used in order to compute the directional fluxes and the model is normalized by the measured omnidirectional flux. Denoting the PAD model as $\hat{j}(E,\alpha_{eq})$, the modeled directional flux is thus

$$j(E,\alpha_{eq}) = N(E)\hat{j}(E,\alpha_{eq}) \tag{A3}$$

where the energy-dependent normalization $N(E)$ can be solved using the equations presented above. Additionally, a change of variables is needed to integrate over the equatorial PAD since Eq. A1 is expressed in terms of the local pitch angle. We thus have

$$J(E) = N(E)\frac{B}{2B_{eq}}\int_0^{\alpha_{90}} \hat{j}(E,\alpha_{eq})\frac{\sin(2\alpha_{eq})}{\sqrt{1-\frac{B}{B_{eq}}\sin^2(\alpha_{eq})}}d\alpha_{eq} \tag{A4}$$

where B and B_{eq} are the local and equatorial magnetic field magnitudes, respectively, and the integration limit is the equatorial pitch angle corresponding to local 90° pitch angle solved from the conservation of the first adiabatic invariant as

$$\alpha_{90} = \arcsin\left(\sqrt{\frac{B_{eq}}{B}}\right). \tag{A5}$$

By computing the integral in Eq. A4, we can solve the normalization at each energy and time step, as $J(E)$ is known from observations, and thus solve the directional flux from Eq. A3.

As discussed in the main text, if the equatorial pitch angle range observable by the GPS satellite is limited, there is more uncertainty in the directional fluxes especially near the equator. Depending on the shape of the PAD and how small the highest observable equatorial pitch angle α_{90} is, the above described normalization can be based on only a small part of the full PAD which might lead to poor PAD fitting and fluctuations in the derived PSD. Thus, we calculate the ratio of the PAD integral over the part GPS can measure to the integral over the full PAD:

$$\frac{I_{GPS}}{I_{tot}} = \frac{\int_0^{\alpha_{90}} \hat{j}(E, \alpha_{eq}) \sin(\alpha_{eq}) d\alpha_{eq}}{\int_0^{\pi/2} \hat{j}(E, \alpha_{eq}) \sin(\alpha_{eq}) d\alpha_{eq}}. \tag{A6}$$

In this paper, data are discarded if the ratio is below 10%.

Acknowledgments

We gratefully acknowledge the Finnish Centre of Excellence in Research of Sustainable Space (Academy of Finland grant 1312390). MMHK gratefully acknowledges the Los Alamos National Laboratory for the Vela Fellowship which enabled this study. Contributions to this work by MGH and SKM were performed under the auspices of the U.S. Department of Energy. EKJK acknowledges the European Research Council (ERC) under the European Union's Horizon 2020 Research and Innovation Programme Project SolMAG 724391, and Academy of Finland project 1310445. AO acknowledges funding from the Academy of Finland by the profiling action on Matter and Materials, grant No. 318913. The work of LT is supported by the Academy of Finland (grant 322544). MP acknowledges ERC under the European Union's Horizon 2020 Research and Innovation Programme Project 682068-PRESTISSIMO, and Academy of Finland project 312351. The authors wish to thank the Finnish Grid and Cloud Infrastructure for supporting this project with computational resources.

We gratefully acknowledge the CXD team at Los Alamos National Laboratory for designing, building and operating the CXD instruments, and for supporting open science by making the data products publicly available (`https://www.ngdc.noaa.gov/stp/space-weather/satellite-data/satellite-systems/gps/`). The authors are also thankful to all of the Van Allen Probes and OMNI teams for making their data available to the public. We thank Harlan Spence and the ECT team for Van Allen Probes MagEIS and REPT electron flux data (`https://rbsp-ect.newmexicoconsortium.org/science/DataDirectories.php`) and Craig Kletzing and the EMFISIS team for Van Allen Probes wave data (`https://emfisis.physics.uiowa.edu/data/index`). The OMNI data were obtained through CDAWeb (`https://cdaweb.sci.gsfc.nasa.gov/index.html/`).

MMHK performed the analysis under the supervision of MGH, SKM, EKJK and AO. LO provided the code to run the geomagnetic field model. MMHK interpreted the results and prepared the manuscript with contributions from all authors.

References

Aseev, N. A., Shprits, Y. Y., Drozdov, A. Y., Kellerman, A. C., Usanova, M. E., Wang, D., & Zhelavskaya, I. S. (2017, October). Signatures of Ultrarelativistic Electron Loss in the Heart of the Outer Radiation Belt Measured by Van Allen Probes. *J. Geophys. Res. Space Physics*, *122*(10), 10,102-10,111. doi: 10.1002/2017JA024485

Baker, D. N., Jaynes, A. N., Li, X., Henderson, M. G., Kanekal, S. G., Reeves, G. D., ... Shprits, Y. Y. (2014, Mar). Gradual diffusion and punctuated phase space density enhancements of highly relativistic electrons: Van Allen Probes observations. *Geophys. Res. Lett.*, *41*(5), 1351-1358. doi: 10.1002/2013GL058942

Baker, D. N., Kanekal, S. G., Hoxie, V. C., Batiste, S., Bolton, M., Li, X., ... Friedel, R. (2013, Nov). The Relativistic Electron-Proton Telescope (REPT) Instrument on Board the Radiation Belt Storm Probes (RBSP) Spacecraft: Characterization of Earth's Radiation Belt High-Energy Particle Populations. *Space Sci. Rev.*, *179*(1-4), 337-381. doi: 10.1007/s11214-012-9950-9

Blake, J. B., Carranza, P. A., Claudepierre, S. G., Clemmons, J. H., Crain, W. R., Dotan, Y., ... Zakrzewski, M. P. (2013, Nov). The Magnetic Electron Ion Spectrometer (MagEIS) Instruments Aboard the Radiation Belt Storm Probes (RBSP) Spacecraft. *Space Sci. Rev.*, *179*(1-4), 383-421. doi: 10.1007/s11214-013-9991-8

Boyd, A. J., Turner, D. L., Reeves, G. D., Spence, H. E., Baker, D. N., & Blake, J. B. (2018, June). What Causes Radiation Belt Enhancements: A Survey of the Van Allen Probes Era. *Geophys. Res. Lett.*, *45*(11), 5253-5259. doi: 10.1029/2018GL077699

Chen, Y., Friedel, R. H. W., Henderson, M. G., Claudepierre, S. G., Morley, S. K., & Spence, H. E. (2014, March). REPAD: An empirical model of pitch angle distributions for energetic electrons in the Earth's outer radiation belt. *J. Geophys. Res. Space Physics*, *119*(3), 1693-1708. doi: 10.1002/2013JA019431

Chen, Y., Friedel, R. H. W., Reeves, G. D., Onsager, T. G., & Thomsen, M. F. (2005, Oct). Multisatellite determination of the relativistic electron phase space density at geosynchronous orbit: Methodology and results during geomagnetically quiet times. *J. Geophys. Res. Space Physics*, *110*(A10), A10210. doi: 10.1029/2004JA010895

Chen, Y., Reeves, G. D., & Friedel, R. H. W. (2007, Sep). The energization of relativistic electrons in the outer Van Allen radiation belt. *Nat. Phys.*, *3*(9), 614-617. doi: 10.1038/nphys655

Da Silva, L. A., Shi, J., Alves, L. R., Sibeck, D., Souza, V. M., Marchezi, J. P., ... Kanekal, S. G. (2020). Dynamic Mechanisms Associated With High-Energy Electron Flux Dropout in the Earth's Outer Radiation Belt Under the Influence of a Coronal Mass Ejection Sheath Region. *J. Geophys. Res. Space Physics*, *126*(1), e2020JA028492. Retrieved from `https://agupubs.onlinelibrary.wiley.com/doi/abs/10.1029/2020JA028492` doi: 10.1029/2020JA028492

Green, J. C., & Kivelson, M. G. (2004, Mar). Relativistic electrons in the outer radiation belt: Differentiating between acceleration mechanisms. *J. Geophys. Res. Space Physics*, *109*(A3), A03213. doi: 10.1029/2003JA010153

Hartley, D. P., & Denton, M. H. (2014, December). Solving the radiation belt riddle. *Astronomy and Geophysics*, *55*(6), 6.17-6.20. doi: 10.1093/astrogeo/atu247

Henderson, M., Morley, S., Niehof, J., & Larsen, B. (2018, March). *drsteve/LANLGeoMag: v1.5.16.* Zenodo. doi: 10.5281/zenodo.1195041

Hess, W. N. (1968). *The radiation belt and magnetosphere.* Blaisdell Publishing Company. (p. 65)

Hietala, H., Kilpua, E. K. J., Turner, D. L., & Angelopoulos, V. (2014, Apr). Depleting effects of ICME-driven sheath regions on the outer electron radiation belt. *Geophys. Res. Lett.*, *41*(7), 2258-2265. doi: 10.1002/2014GL059551

Jaynes, A. N., Baker, D. N., Singer, H. J., Rodriguez, J. V., Loto'aniu, T. M., Ali, A. F., ... Reeves, G. D. (2015, Sep). Source and seed populations for relativistic electrons: Their roles in radiation belt changes. *J. Geophys. Res. Space Physics*, *120*(9), 7240-7254. doi: 10.1002/2015JA021234

Kalliokoski, M. M. H., Kilpua, E. K. J., Osmane, A., Jaynes, A. N., Turner, D. L., George, H., ... Palmroth, M. (2022). Phase space density analysis of outer radiation belt electron energization and loss during geoeffective and nongeoeffective sheath regions. *J. Geophys. Res. Space Physics*, *127*(3), e2021JA029662. doi: https://doi.org/10.1029/2021JA029662

Kalliokoski, M. M. H., Kilpua, E. K. J., Osmane, A., Turner, D. L., Jaynes, A. N., Turc, L., ... Palmroth, M. (2020, June). Outer radiation belt and inner magnetospheric response to sheath regions of coronal mass ejections: a statistical analysis. *Ann. Geophys.*, *38*(3), 683-701. doi: 10.5194/angeo-38-683-2020

Kennel, C. F., & Petschek, H. E. (1966, January). Limit on Stably Trapped Particle Fluxes. *J. Geophys. Res.*, *71*, 1. doi: 10.1029/JZ071i001p00001

Kilpua, E. K. J., Balogh, A., von Steiger, R., & Liu, Y. D. (2017, November). Geoeffective Properties of Solar Transients and Stream Interaction Regions. *Space Sci. Rev.*, *212*, 1271-1314. doi: 10.1007/s11214-017-0411-3

Kilpua, E. K. J., Fontaine, D., Moissard, C., Ala-Lahti, M., Palmerio, E., Yordanova, E., ... Turc, L. (2019, Jul). Solar wind properties and geospace impact of coronal mass ejection-driven sheath regions: Variation and driver dependence. *Space Weather*, *17*(0). doi: 10.1029/2019SW002217

Kilpua, E. K. J., Hietala, H., Turner, D. L., Koskinen, H. E. J., Pulkkinen, T. I., Rodriguez, J. V., ... Spence, H. E. (2015, May). Unraveling the drivers of the storm time radiation belt response. *Geophys. Res. Lett.*, *42*(9), 3076-3084. doi: 10.1002/2015GL063542

Kilpua, E. K. J., Koskinen, H. E. J., & Pulkkinen, T. I. (2017, Nov). Coronal mass ejections and their sheath regions in interplanetary space. *Living Rev. Sol. Phys.*, *14*(1), 5. doi: 10.1007/s41116-017-0009-6

Kilpua, E. K. J., Turner, D. L., Jaynes, A. N., Hietala, H., Koskinen, H. E. J., Osmane, A., ... Claudepierre, S. G. (2019, Mar). Outer Van Allen Radiation Belt Response to Interacting Interplanetary Coronal Mass Ejections. *J. Geophys. Res. Space Physics*, *124*(3), 1927-1947. doi: 10.1029/2018JA026238

Kim, H.-J., & Chan, A. A. (1997, September). Fully adiabatic changes in storm time relativistic electron fluxes. *J. Geophys. Res.*, *102*(A10), 22107-22116. doi: 10.1029/97JA01814

Kim, H. J., Lee, D. Y., Wolf, R., Bortnik, J., Kim, K. C., Lyons, L., ... Li, J. (2021, May). Rapid Injections of MeV Electrons and Extremely Fast Step Like Outer Radiation Belt Enhancements. *Geophys. Res. Lett.*, *48*(9), e93151. doi: 10.1029/2021GL093151

Kletzing, C. A., Kurth, W. S., Acuna, M., MacDowall, R. J., Torbert, R. B., Averkamp, T., ... Tyler, J. (2013, Nov). The Electric and Magnetic Field Instrument Suite and Integrated Science (EMFISIS) on RBSP. *Space Sci. Rev.*, *179*(1-4), 127-181. doi: 10.1007/s11214-013-9993-6

Kurita, S., Miyoshi, Y., Shiokawa, K., Higashio, N., Mitani, T., Takashima, T., ... Otsuka, Y. (2018, December). Rapid Loss of Relativistic Electrons by EMIC Waves in the Outer Radiation Belt Observed by Arase, Van Allen Probes, and the PWING Ground Stations. *Geophys. Res. Lett.*, *45*(23), 12,720-12,729. doi: 10.1029/2018GL080262

Mauk, B. H., Fox, N. J., Kanekal, S. G., Kessel, R. L., Sibeck, D. G., & Ukhorskiy, A. (2013, Nov). Science Objectives and Rationale for the Radiation Belt Storm Probes Mission. *Space Sci. Rev.*, *179*(1-4), 3-27. doi: 10.1007/s11214-012-9908-y

McIlwain, C. E. (1961, Nov). Coordinates for Mapping the Distribution of Magnetically Trapped Particles. *J. Geophys. Res.*, *66*(11), 3681-3691. doi: 10.1029/JZ066i011p03681

Miyoshi, Y., Kataoka, R., Kasahara, Y., Kumamoto, A., Nagai, T., & Thomsen, M. F. (2013, September). High-speed solar wind with southward interplanetary magnetic field causes relativistic electron flux enhancement of the outer radiation belt via enhanced condition of whistler waves. *Geophys. Res. Lett.*,

40(17), 4520-4525. doi: 10.1002/grl.50916
Morley, S. K., Friedel, R. H. W., Cayton, T. E., & Noveroske, E. (2010, March). A rapid, global and prolonged electron radiation belt dropout observed with the Global Positioning System constellation. *Geophys. Res. Lett.*, *37*(6), L06102. doi: 10.1029/2010GL042772
Morley, S. K., Friedel, R. H. W., Spanswick, E. L., Reeves, G. D., Steinberg, J. T., Koller, J., … Noveroske, E. (2010, November). Dropouts of the outer electron radiation belt in response to solar wind stream interfaces: global positioning system observations. *Proc. R. Soc. A*, *466*(2123), 3329-3350. doi: 10.1098/rspa.2010.0078
Morley, S. K., Henderson, M. G., Reeves, G. D., Friedel, R. H. W., & Baker, D. N. (2013, September). Phase Space Density matching of relativistic electrons using the Van Allen Probes: REPT results. *Geophys. Res. Lett.*, *40*(18), 4798-4802. doi: 10.1002/grl.50909
Morley, S. K., Sullivan, J. P., Carver, M. R., Kippen, R. M., Friedel, R. H. W., Reeves, G. D., & Henderson, M. G. (2017, February). Energetic Particle Data From the Global Positioning System Constellation. *Space Weather*, *15*(2), 283-289. doi: 10.1002/2017SW001604
Morley, S. K., Sullivan, J. P., Henderson, M. G., Blake, J. B., & Baker, D. N. (2016, February). The Global Positioning System constellation as a space weather monitor: Comparison of electron measurements with Van Allen Probes data. *Space Weather*, *14*(2), 76-92. doi: 10.1002/2015SW001339
Morley, S. K., Sullivan, J. P., Schirato, R. C., & Terry, J. R. (2014). *Data processing for energetic particle measurements from the Global Positioning System (GPS) constellation* (Tech. Rep. No. LA-UR-14-28961). Los Alamos, NM: Los Alamos National Laboratory. doi: 10.2172/1164428
Moya, P. S., Pinto, V. A., Sibeck, D. G., Kanekal, S. G., & Baker, D. N. (2017, Nov). On the Effect of Geomagnetic Storms on Relativistic Electrons in the Outer Radiation Belt: Van Allen Probes Observations. *J. Geophys. Res. Space Physics*, *122*(11), 11,100-11,108. doi: 10.1002/2017JA024735
O'Brien, T. P., McPherron, R. L., Sornette, D., Reeves, G. D., Friedel, R., & Singer, H. J. (2001, Aug). Which magnetic storms produce relativistic electrons at geosynchronous orbit? *J. Geophys. Res.*, *106*(A8), 15533-15544. doi: 10.1029/2001JA000052
Olifer, L., Mann, I. R., Morley, S. K., Ozeke, L. G., & Choi, D. (2018, May). On the Role of Last Closed Drift Shell Dynamics in Driving Fast Losses and Van Allen Radiation Belt Extinction. *J. Geophys. Res. Space Physics*, *123*(5), 3692-3703. doi: 10.1029/2018JA025190
Olifer, L., Mann, I. R., Ozeke, L. G., Morley, S. K., & Louis, H. L. (2021, June). On the Formation of Phantom Electron Phase Space Density Peaks in Single Spacecraft Radiation Belt Data. *Geophys. Res. Lett.*, *48*(11), e92351. doi: 10.1029/2020GL092351
Pulkkinen, T. I., Partamies, N., Huttunen, K. E. J., Reeves, G. D., & Koskinen, H. E. J. (2007, January). Differences in geomagnetic storms driven by magnetic clouds and ICME sheath regions. *Geophys. Res. Lett.*, *34*(2), L02105. doi: 10.1029/2006GL027775
Reeves, G. D., McAdams, K. L., Friedel, R. H. W., & O'Brien, T. P. (2003, May). Acceleration and loss of relativistic electrons during geomagnetic storms. *Geophys. Res. Lett.*, *30*(10), 1529. doi: 10.1029/2002GL016513
Reeves, G. D., Spence, H. E., Henderson, M. G., Morley, S. K., Friedel, R. H. W., Funsten, H. O., … Niehof, J. T. (2013, Aug). Electron Acceleration in the Heart of the Van Allen Radiation Belts. *Science*, *341*(6149), 991-994. doi: 10.1126/science.1237743
Roederer, J. G. (1970). *Dynamics of geomagnetically trapped radiation.* Berlin, Heidelberg: Springer-Verlag. doi: 10.1007/978-3-642-49300-3

Shprits, Y. Y., Kellerman, A., Aseev, N., Drozdov, A. Y., & Michaelis, I. (2017, Feb). Multi-MeV electron loss in the heart of the radiation belts. *Geophys. Res. Lett.*, *44*(3), 1204-1209. doi: 10.1002/2016GL072258

Smirnov, A. G., Berrendorf, M., Shprits, Y. Y., Kronberg, E. A., Allison, H. J., Aseev, N. A., ... Effenberger, F. (2020, November). Medium Energy Electron Flux in Earth's Outer Radiation Belt (MERLIN): A Machine Learning Model. *Space Weather*, *18*(11), e02532. doi: 10.1029/2020SW002532

Spence, H. E., Reeves, G. D., Baker, D. N., Blake, J. B., Bolton, M., Bourdarie, S., ... Thorne, R. M. (2013, November). Science Goals and Overview of the Radiation Belt Storm Probes (RBSP) Energetic Particle, Composition, and Thermal Plasma (ECT) Suite on NASA's Van Allen Probes Mission. *Space Sci. Rev.*, *179*, 311-336. doi: 10.1007/s11214-013-0007-5

Tsyganenko, N. A., & Sitnov, M. I. (2005, Mar). Modeling the dynamics of the inner magnetosphere during strong geomagnetic storms. *J. Geophys. Res. Space Physics*, *110*(A3), A03208. doi: 10.1029/2004JA010798

Turner, D. L., Angelopoulos, V., Li, W., Bortnik, J., Ni, B., Ma, Q., ... Rodriguez, J. V. (2014, Mar). Competing source and loss mechanisms due to wave-particle interactions in Earth's outer radiation belt during the 30 September to 3 October 2012 geomagnetic storm. *J. Geophys. Res. Space Physics*, *119*(3), 1960-1979. doi: 10.1002/2014JA019770

Turner, D. L., Cohen, I. J., Michael, A., Sorathia, K., Merkin, S., Mauk, B. H., ... Reeves, G. D. (2021, November). Can Earth's Magnetotail Plasma Sheet Produce a Source of Relativistic Electrons for the Radiation Belts? *Geophys. Res. Lett.*, *48*(21), e95495. doi: 10.1029/2021GL095495

Turner, D. L., Kilpua, E. K. J., Hietala, H., Claudepierre, S. G., O'Brien, T. P., Fennell, J. F., ... Reeves, G. D. (2019, February). The Response of Earth's Electron Radiation Belts to Geomagnetic Storms: Statistics From the Van Allen Probes Era Including Effects From Different Storm Drivers. *J. Geophys. Res. Space Physics*, *124*, 1013-1034. doi: 10.1029/2018JA026066

Turner, D. L., O'Brien, T. P., Fennell, J. F., Claudepierre, S. G., Blake, J. B., Kilpua, E. K. J., & Hietala, H. (2015, November). The effects of geomagnetic storms on electrons in Earth's radiation belts. *Geophys. Res. Lett.*, *42*, 9176-9184. doi: 10.1002/2015GL064747

Turner, D. L., Shprits, Y., Hartinger, M., & Angelopoulos, V. (2012, Mar). Explaining sudden losses of outer radiation belt electrons during geomagnetic storms. *Nat. Phys.*, *8*(3), 208-212. doi: 10.1038/nphys2185

Turner, D. L., & Ukhorskiy, A. Y. (2020). Chapter 1 - Outer radiation belt losses by magnetopause incursions and outward radial transport: new insight and outstanding questions from the Van Allen Probes era. In A. N. Jaynes & M. E. Usanova (Eds.), *The Dynamic Loss of Earth's Radiation Belts* (p. 1-28). Elsevier. Retrieved from `http://www.sciencedirect.com/science/article/pii/B9780128133712000019` doi: 10.1016/B978-0-12-813371-2.00001-9

Tuszewski, M., Cayton, T. E., Ingraham, J. C., & Kippen, R. M. (2004, October). Bremsstrahlung effects in energetic particle detectors. *Space Weather*, *2*(10), S10S01. doi: 10.1029/2003SW000057